RESEARCH

Structural, thermal, surface, and electrical properties of Bi_2O_3 ceramics co–doped with Er–Ho–Tb rare earths

Murat Balci[1]

Abstract

Face–centered cubic–Bi_2O_3 (δ–phase) material is a better ion conductor when compared to other types of solid electrolytes that have been declared in the literature due to its anion–defective crystal configuration, and hence it can be a promising solid electrolyte choice for intermediate temperature SOFC applications. In this research, Er–Ho–Tb co–doped Bi_2O_3 compounds were successfully synthesized by the solid–state reaction method and characterized using the XRD, TG & DTA, FPPT, and FE–SEM techniques. Apart from sample 4Er4Ho4Tb, each sample became stable with a cubic δ–phase at room temperature, according to XRD patterns. The DTA curves revealed no exothermic or endothermic peaks, implying a phase change in the constant heating cycle. The conductivity of Ho–rich compositions was higher than that of others, confirming the impact of cation polarizability on conductivity. In addition, at 700 °C, the sample 4Er8Ho4Tb with 1:2:1 content ratios had the highest conductivity of 0.29 S/cm. The porosity on the grain boundaries increased with doping, leading to higher grain boundary resistance, which could be responsible for the conductivity drop.

Keywords Phase transition · X–Ray diffraction · Lattice shrinkage · Grain size · Differential thermal analysis

Introduction

High Temperature–Solid Oxide Fuel Cells (HT–SOFCs) are alternative energy sources that are able to generate electrical energy electrochemically. The primary advantages of this cell type are its environmentally friendly functioning in terms of principle, along with its extremely high electricity efficiency, which can reach up to 85% [1, 2]. However, the high operating temperature (> 800 °C) challenges these batteries over time, causing the electrode–electrolyte interface to deteriorate, resulting in a sudden decrease in the cell's open circuit voltage (OCV) and reducing battery life. Therefore, significant attempts have been made in recent years to lower the operating temperature of SOFCs to intermediate (500–700 °C) and low temperatures (< 500 °C) [3–5]. The low temperature also leads to two key issues that reduce the electricity efficiency of the cell: the slowing of kinetic processes at the electrode–electrolyte interfaces and a drop in

the ion conductivity of the currently used Yttria–stabilized zirconia (YSZ) electrolyte. To compensate for the significant reduction in cell efficiency, materials with higher ion conductivity than YSZ can be developed for low temperature SOFC technology [6].

Bismuth (III) Oxide (Bi_2O_3), with its face–centered cubic crystal structure (δ–phase), can be a promising solid electrolyte option for SOFC units since it has extremely strong oxygen–ion conductivity at comparable temperatures to YSZ–type electrolytes [7, 8]. When driven to intermediate temperatures (< 729 °C), this cubic phase somehow transforms into other bismuth oxide phases exhibiting lower ion conductivity than that of it, such as monoclinic α–phase, and is therefore classified as a metastable phase. Nevertheless, recently published studies have shown that cubic δ–phase can be maintained at all temperatures, including room temperature, by doping certain rare earth cations into pure Bi_2O_3 crystals using a variety of experimental methods [9–13]. In addition, several doping elements, such as dopant ion radius and concentration, should be taken into account for cubic phase stability in order to attain the ideal phase stability and highest conductivity for doped Bi_2O_3 systems. According to previously published studies, when the rare earth cations that serve as dopants are smaller than the host

✉ Murat Balci
muratbalci@erciyes.edu.tr

1 Department of Physics, Erciyes University, Kayseri 38039, Turkey

Bi^{3+} cation (1.17), the cubic δ–phase can be easily stabilized; otherwise, larger dopants allow for the development of the rhombohedral crystal phase, which has lower ion conductivity than the δ–phase [14]. The conductivity measurements for stabilized δ–phase, on the other hand, indicated that the findings were lower than those for the pure phase. The decrease in conductivity is primarily brought about by a decrease in cation polarizability as a result of partial cation exchange between the host Bi^{3+} and dopant cations (Ln^{3+} ↔ Bi^{3+}). In fact, in oxide–based crystals, cation polarizability can be defined as the strength of a cation to attract an oxygen ion (O^{2-}) in the anion sublattice, and it is usually proportional to the cation's radius [15, 16]. Additionally, it is well known that the Bi^{3+} cation exhibits higher polarizability due to $6s^2$ lone pair electrons, and therefore, the anion sublattice of the pure cubic phase has an anion–defective structure with 75% occupancy. Small–radius cations substituted with Bi^{3+} cations with partial exchange of cations lead to a drop in ion conductivity because of the low polarizing power. Many stabilization investigations employing a variety of rare earth cations as additives have yielded very favorable outcomes for cubic phase stability [17, 18]. The double doping technique, however, achieved the best conductivity for the stable δ–phase. Jung et al. studied cubic phase stabilization by doping with W and Dy cations while maintaining the total dopant concentration at 12%. They obtained an optimal conductivity of 0.487 S/cm at 700 °C in a sample with a doping ratio of 2:1 (W:Dy). Further, they suggested that the total dopant concentration be kept as low as possible in order to attain the highest ion conductivity for the stable cubic phase [19].

In the present study, rare metal oxides Er_2O_3, Ho_2O_3, and Tb_4O_7 were added to pure Bi_2O_3 under air conditions via a series of solid–state processes to stabilize the highly ion–conducting cubic δ–phase at ambient temperature. The developed samples were evaluated structurally, thermally, and on the surface using X–Ray Diffraction (XRD), Thermo–gravimetric and Differential Thermal Analysis (TG & DTA), and Field Emission–Scanning Electron Microscope (FE–SEM), respectively. Conductivity measurements on all materials were taken under an atmosphere using the Four Point Probe Technique (FPPT). The impact of total dopant quantity and content ratios on the structural, thermal, morphologic, and electrical properties of the fabricated samples was thoroughly examined and discussed.

Experimental section

Material synthesis

As starting materials, powders including Bi_2O_3 (>99, 98% purity, Sigma Aldrich), Ho_2O_3 (>98, 90% purity, Sigma Aldrich), Er_2O_3 (>98, 95% purity, Alfa Aesar), and Tb_4O_7 (>98, 90% purity, Sigma Aldrich) were supplied. All powder mixtures were created in the air using solid–state reactions with the proper stoichiometry. The chemical components and fabrication of $(Bi_2O_3)_{1-x-y-z}$ $(Er_2O_3)_x$ $(Ho_2O_3)_y$ $(Tb_4O_7)_z$ systems are summarized in Table 1 and Scheme 1, respectively. The mass values of the powders corresponding to mole ratios were measured using a digital precision scale. Each powder was then carefully ground with a pestle in an agate mortar in order to create a desirable mixture. After manufacturing, all powder samples were thermally treated to guarantee the stability of the cubic δ–phase and the appropriate diffusion of rare earth cations into the pure Bi_2O_3 crystal. In the present study, the annealing temperature was set to 750 °C, which is higher than the phase transition temperature (729 °C), at which the monoclinic α–phase transforms to the cubic δ–phase when heated.

In addition, the annealing time was set at 100 h (about four days) to ensure adequate solidification and a better diffusion process. Around 1200 mg of the powder mixture was used for creating the pallet samples with a 13 mm diameter and a 5 mm thickness to carry out various tests, such as conductivity measurements. The pallets were created using a pressing machine capable of producing around 10 tons of pressure in an axial arrangement.

Table 1 Molar ratios of the $(Bi_2O_3)_{1-x-y-z}$ $(Er_2O_3)_x$ $(Ho_2O_3)_y$ $(Tb_4O_7)_z$ systems

Compositions	Sample abbreviation	Content ratios (Er : Ho : Tb)	Total dopant concentration (mol %)
$(Bi_2O_3)_{0.88}$ $(Er_2O_3)_{0.04}$ $(Ho_2O_3)_{0.04}$ $(Tb_4O_7)_{0.04}$	4Er4Ho4Tb	1:1:1	12
$(Bi_2O_3)_{0.84}$ $(Er_2O_3)_{0.08}$ $(Ho_2O_3)_{0.04}$ $(Tb_4O_7)_{0.04}$	8Er4Ho4Tb	2:1:1	16
$(Bi_2O_3)_{0.80}$ $(Er_2O_3)_{0.12}$ $(Ho_2O_3)_{0.04}$ $(Tb_4O_7)_{0.04}$	12Er4Ho4Tb	3:1:1	20
$(Bi_2O_3)_{0.76}$ $(Er_2O_3)_{0.16}$ $(Ho_2O_3)_{0.04}$ $(Tb_4O_7)_{0.04}$	16Er4Ho4Tb	4:1:1	24
$(Bi_2O_3)_{0.84}$ $(Er_2O_3)_{0.04}$ $(Ho_2O_3)_{0.08}$ $(Tb_4O_7)_{0.04}$	4Er8Ho4Tb	1:2:1	16
$(Bi_2O_3)_{0.80}$ $(Er_2O_3)_{0.04}$ $(Ho_2O_3)_{0.12}$ $(Tb_4O_7)_{0.04}$	4Er12Ho4Tb	1:3:1	20
$(Bi_2O_3)_{0.76}$ $(Er_2O_3)_{0.04}$ $(Ho_2O_3)_{0.16}$ $(Tb_4O_7)_{0.04}$	4Er16Ho4Tb	1:4:1	24
$(Bi_2O_3)_{0.84}$ $(Er_2O_3)_{0.04}$ $(Ho_2O_3)_{0.04}$ $(Tb_4O_7)_{0.08}$	4Er4Ho8Tb	1:1:2	16
$(Bi_2O_3)_{0.80}$ $(Er_2O_3)_{0.04}$ $(Ho_2O_3)_{0.04}$ $(Tb_4O_7)_{0.12}$	4Er4Ho12Tb	1:1:3	20
$(Bi_2O_3)_{0.76}$ $(Er_2O_3)_{0.04}$ $(Ho_2O_3)_{0.04}$ $(Tb_4O_7)_{0.16}$	4Er4Ho16Tb	1:1:4	24

Scheme 1 Fabrication of the $(Bi_2O_3)_{1-x-y-z}$ $(Er_2O_3)_x$ $(Ho_2O_3)_y$ $(Tb_4O_7)_z$ compositions
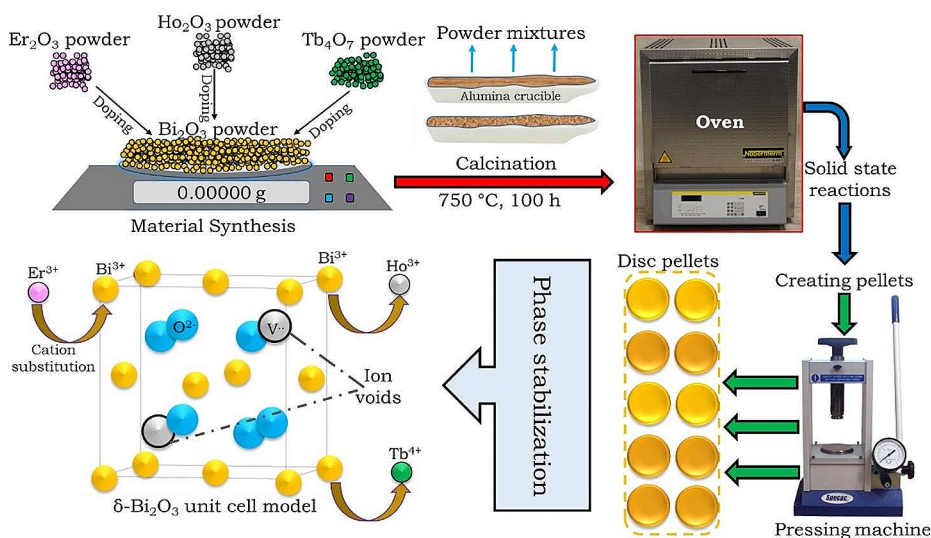
Characterization

The XRD experiments were performed at room temperature using a Panalytical Empyrean Model Diffractometer with Cu–K$_\alpha$ radiation at a wavelength of 1.54 Å and a scanning step of 0.02 °/sec from 10° to 90°. The Diamond TG & DTA Perkin Elmer equipment was used to explore temperature–dependent thermal events such as phase transition and mass loss. The heating rate was adjusted at 10 °C/min to precisely observe endothermic or exothermic peaks on the DTA curves, indicating a probable phase transition. Morphological properties, such as grain size and boundary, were investigated by employing the ZEISS Gemini SEM 500 model Field–Emission Scanning Electron Microscopy (FE–SEM) at room temperature. The electrical conductivity of all samples was measured with the Four Point Probe Technique (FPPT), which allows for reliable resistivity measurement without requiring the presence of extra resistivity, such as contact resistance. The conductivity tests were carried out in a programmable ash furnace using a specially designed alumina kit system, a Keithley 2700 model multimeter, and a Keithley 2400 model D.C. power supply. Throughout the experiment, the furnace temperature was gradually increased from room temperature to a high temperature (1000 °C) using a constant heating step (10 °C/min).

Results and discussion

The conventional XRD patterns of the samples and magnified XRD representations of the main diffraction peak belonging to the (111) plane are shown in Fig. 1. Based on the recorded peak locations, it is obvious that, except for sample 4Er4Ho4Tb, all samples are stabilized with the cubic δ–phase at room temperature, according to ICDD

reference code: 00–041–0283. The appearance of both α– and δ–peaks on the diffraction pattern suggests that sample 4Er4Ho4Tb has a mixed phase structure, as confirmed by the 01–078–1793 ICDD reference code [20]. The Bragg angles at which the minor peaks on the pattern appear are $2\theta = 26.092°$, $2\theta = 27.150°$, $2\theta = 28.821°$, $2\theta = 30.926°$, and $2\theta = 50.782°$. Also, Bragg angles for the stabilized δ–phase were identified to be $2\theta = 28.087°$ (111), $2\theta = 32.655°$ (200), $2\theta = 46.517$ (220), and $2\theta = 55.461°$ (311). $2\theta = 58.186°$ (222), $2\theta = 68.732°$ (400), $2\theta = 75.068°$ (331), $2\theta = 77.051°$ (420), and $2\theta = 86.913°$ (422). It can be observed that when the doping rate increases, the minor peaks related to the mixed phase on the spectrum disappear and only the diffraction peaks associated with the cubic δ–phase remain. In reality, this finding demonstrates that rare earth cations, which are all smaller than the host cation, experience partial cationic substitution. As a result of this, the lattice stress reaches a level that prevents the crystal phase transition from the δ–phase to the α–phase or other phases.

When the magnified XRD patterns are closely examined, a change in the position of the primary peak can be easily noticed. With the exception of sample 8Er4Ho4Tb, primary peaks on the diffraction pattern move to the right as dopant concentrations are progressively raised. This shifting in XRD peaks is mostly considered a reflection of the change in the lattice constant caused by doping–induced impurities. Besides that, the type of peak shifting, which is strongly connected to the broadening or sharpening of the XRD peaks, may lead to an increase or decrease in crystallite size as dopant concentration increases [21, 22]. According to the literature, peak shifts on the diffraction pattern may typically imply an increase in crystal size when it is at larger angles and a decrease when it is at smaller ones. As a matter of fact, when the doping concentration increases, the average crystallite size tends to decrease, implying that the
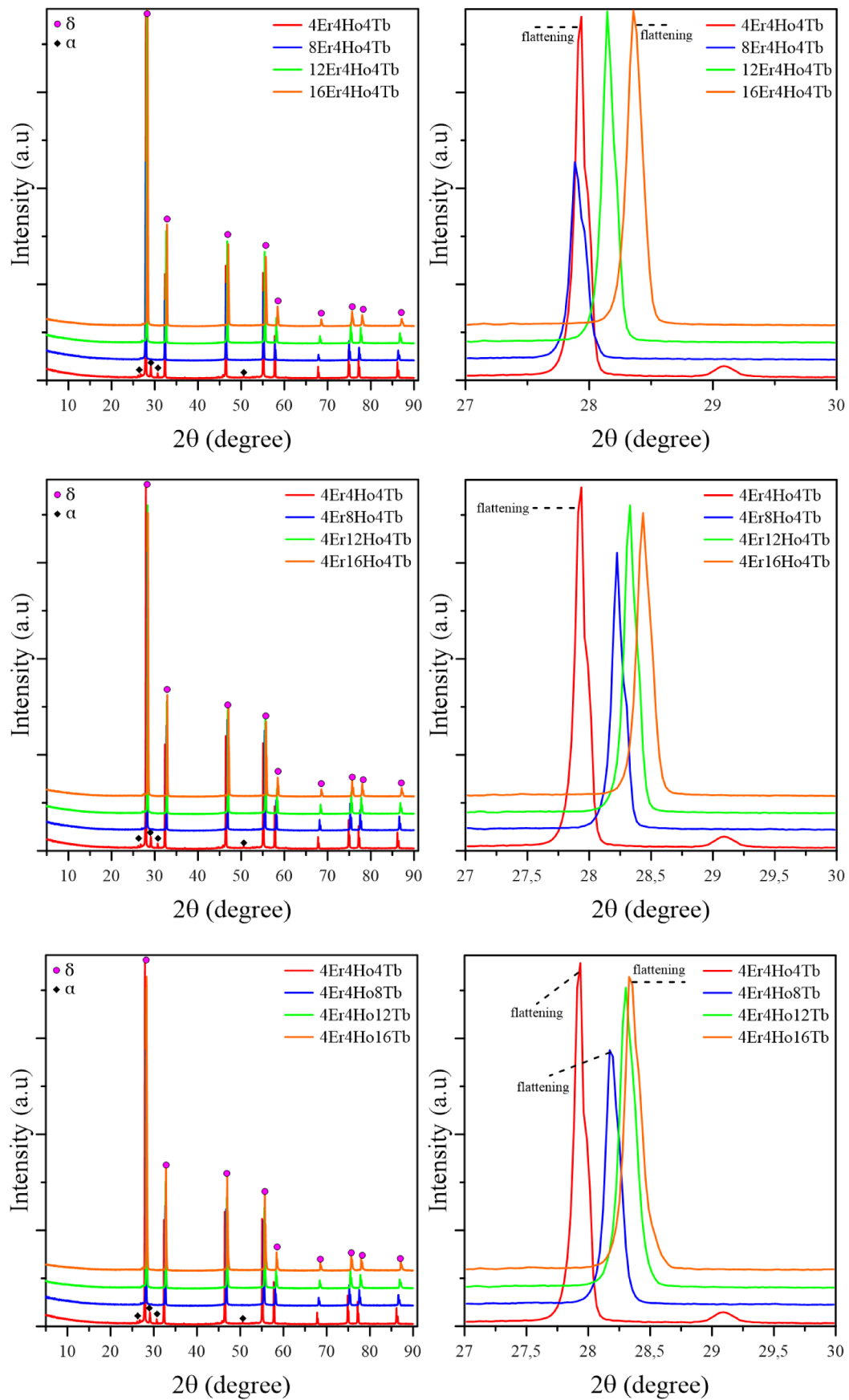
Fig. 1 Stacked XRD patterns including standard and magnified versions at room temperature

crystallinity of the material decreases. Also, peak flattening can be clearly seen in the magnified XRD patterns, which becomes apparent as doping concentration increases [23]. The peak flattening or broadening observed on the XRD pattern can be attributed to the microstrain that develops depending on the doping concentration. In reality, it is not only affected by the concentration of dopants in the lattice but also by the type of dopant and the dopant content ratio [24].

The average crystal size is obtained using the Scherrer formula, which is expressed by the following Eq.

$$D = \frac{k\lambda}{\beta cos\theta} \tag{1}$$

In Eq. (1), k is the shape factor given as about 0.9, λ is the x–ray wavelength, β is the full–width half maxima (Fwhm), and θ is the Bragg diffraction angle. In here, β can be defined by the following Eq.

$$\beta^2 = \beta_m^2 - \beta_s^2 \tag{2}$$

In Eq. (2), β_m is the corrected Fwhm value and β_s represents the contributions arising from reflections.

In addition, the microstrain (ε), which is closely related to the lattice strain, is obtained by using Stokes–Wilson formula given by the following Eq.

$$\beta cos\theta = \epsilon \left(sin\theta\right) + \frac{K\lambda}{D} \tag{3}$$

It is widely known that the degree of impurities added to the pure crystal structure affects crystal size and microstrain. As a result, rare earth cations added to the lattice in this study led to a variation in the crystal lattice parameters [25]. The lattice parameters for cubic δ–phase stabilized samples were estimated by X–Powder and Win–Index software over standard XRD patterns, and the results are summarized in Table 2. As seen in Table 2, as dopant concentration increases, crystal size decreases while microstrain increases. This is an expected result since all rare earth cations did not

effectively experience cationic replacement in other crystal positions, which results in an increase in dislocations in the lattice. These dislocations allow microstrain effects to develop throughout the crystal, driving the crystalline size to shrink, which is sometimes seen in diffraction patterns such as peak broadening [26].

Figure 2a also shows the change in crystalline size and microstrain as a function of Ho_2O_3 mole%. In agreement with earlier studies, the crystal size and the microstrain exhibit a linear relationship with the Ho_2O_3 molar ratio, as seen in this figure. Table 2 also shows that the calculated lattice constants are less than those of the pure cubic fcc phase (5.65 Å). This is not surprising due to the small dopant radius compared to the host Bi^{3+} cation and shows that cation substitution induced by the diffusional process is partially successful. In the literature, this is known as lattice shrinkage and is a common result in stability studies of the cubic phase.

Figure 2b also shows how the lattice constant varies with the total dopant concentration in the composition. This figure clearly indicates that as the active diffusion of rare earth cations into pure Bi_2O_3 increases, the lattice constant decreases as expected [27]. The largest lattice constant is found in Er–rich samples, although Er^{3+} has a larger ion radius than the other cations, Ho^{3+} and Tb^{4+}. This discrepancy could be explained by the fact that the diffusional process induced by solid–state reactions may be effective for Ho^{3+} and Tb^{4+} cations.

Thermal analysis study

The DTA curves of all fabricated samples depending on temperature are shown in Fig. 3a, b, and c. The DTA curves of all samples do not display both exothermic and endothermic peaks, which would suggest a potential phase change. The DTA curve of some samples, such as sample 4Er8Ho4Tb, however, offers minor vibrations that could be attributed to order–disorder transitions rather than phase transitions over a short period of time. It is well known that pure Bi_2O_3 experiences a crystalline phase change from the monoclinic α–phase to the cubic δ–phase at a temperature

Table 2 Structural parameters for the cubic stabilized samples

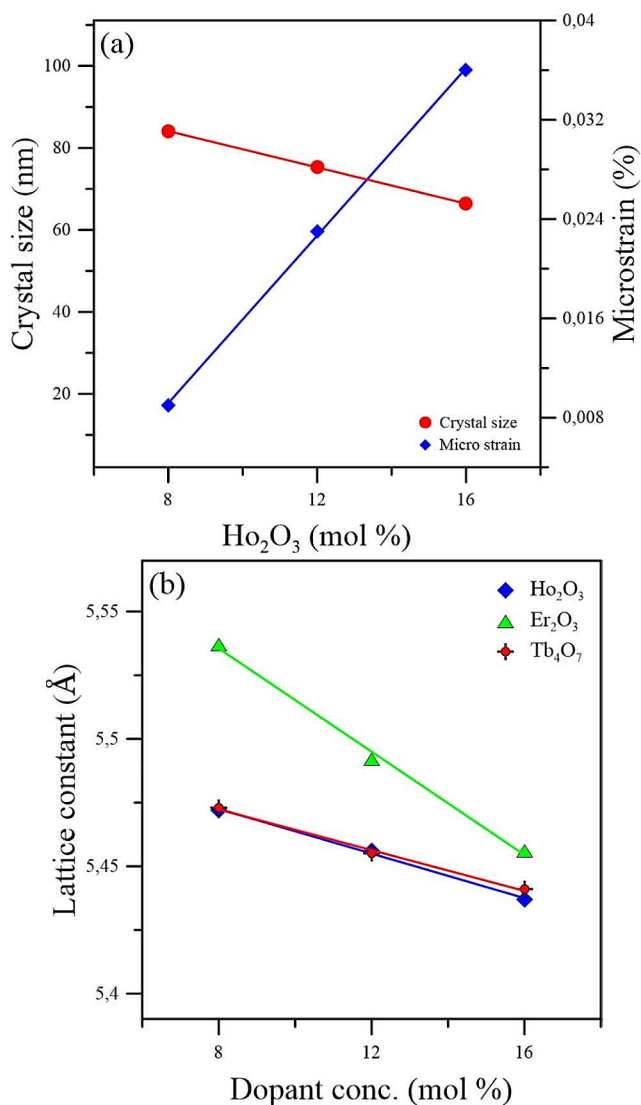| Sample	Crystal size (nm)	Fwhm (°)	Microstrain (%)	Lattice constant (Å)
8Er4Ho4Tb	64.7	0.088	0.041	5.537
12Er4Ho4Tb	74.2	0.050	0.023	5.492
16Er4Ho4Tb	63.9	0.087	0.040	5.456
4Er8Ho4Tb	84.1	0.020	0.009	5.472
4Er12Ho4Tb	75.3	0.050	0.023	5.456
4Er16Ho4Tb	66.4	0.078	0.036	5.437
4Er4Ho8Tb	65.9	0.083	0.038	5.473
4Er4Ho12Tb	61.2	0.094	0.043	5.455
4Er4Ho16Tb	60.7	0.091	0.042	5.441

Fig. 2 **a** Crystal size and microstrain with respect to Ho_2O_3 mol%, **b** Lattice constant versus total dopant concentration

of around 729 °C during the heating cycle [28, 29]. A phase transition in a crystal lattice is a positional evolution of the ions that make up the lattice to the lowest energy, requiring crystal symmetry. Based on the XRD patterns, sample 4Er4Ho4Tb is expected to create an exothermic peak on its DTA curve, implying a possible phase transition from α– to δ–phase. The absence of such a transition on its DTA curve is due to doping elements creating lattice stress–increasing dislocations, blocking an expected transition to the cubic δ– phase. In other words, some rare earth cations that do not undergo partial cation substitution with host Bi^{3+} can operate as stress points in the lattice by settling in various ion regions. In this case, lattice stress may complicate the spatial arrangement necessary for the transition to a new crystal symmetry [30]. Furthermore, the very high heating rate of the thermal analysis instrument (10 °C/min) may obscure

the gathering of these endothermic and exothermic peaks, signaling the phase transition. A further noteworthy finding is the fact that the DTA profiles of some samples exhibit more visible bending at roughly 600 °C, particularly in Ho– rich samples. The literature emphasizes that at this temperature, the doped Bi_2O_3 system undergoes an order–disorder transition (ODT), indicating a positional modification of the O^{2-} ions in the oxygen sublattice. However, ODT is not a change in phase but rather an event that modifies the material's ion conduction mechanism and produces a variation in the energy needed to activate the ions. Put another way, ODT is a positional change of ions that occurs solely in the crystal sublattice, where O2–ions settle. As a result of this transformation, certain ions may move to the 32f octahedral regions. Thus, this transition may have caused the bending or peak creation on the DTA curves.

The TGA curves for Er–rich samples are presented in Fig. 3d. It can be clearly observed from the figure that the weight of specimens varies with temperature, ranging from 1 to 3%. The removal of oxygen from the lattice allows for an increase in the oxygen ion vacancy concentration, which accounts for the majority of temperature–related weight losses in oxide–based systems. Mass losses may also be associated with the evaporation of unwanted impurity atoms during heating.

Additionally, the surveys indicate that there are several possible causes of temperature–induced weight gain. For example, at high temperatures, the measuring atmosphere's density of inert gases, like He, may drop, changing the buoyant force pressing on the sample container. But other things like oxidation, the specimen's surface depositing undesirable pollutants, and rare earth cations absorbing moisture from the surroundings might also be causing the weight to rise [31].

Conductivity measurements

Figure 4 shows the Arrhenius plots of conductivity as a function of temperature for disc–shaped palletized samples. The Arrhenius equation, which is provided in the following formula, describes how electrical conductivity varies with temperature.

$$\sigma_T = \sigma_0 \exp(-\frac{E_A}{k_B T}) \qquad (4)$$

In Eq. (4), σ_T is the conductivity at any temperature, σ_0 is the pre–exponential factor, E_A is the electrical activation energy, and k_B is the Boltzmann constant given as 8.617exp– 05 eV/K. When the logarithm operation is applied to both sides of Eq. (4) in order to observe the linear relationship

Fig. 3 Stacked DTA curves **a** Er–rich samples, **b** Ho–rich samples, **c** Tb–rich samples **d** TG% for Er–rich samples
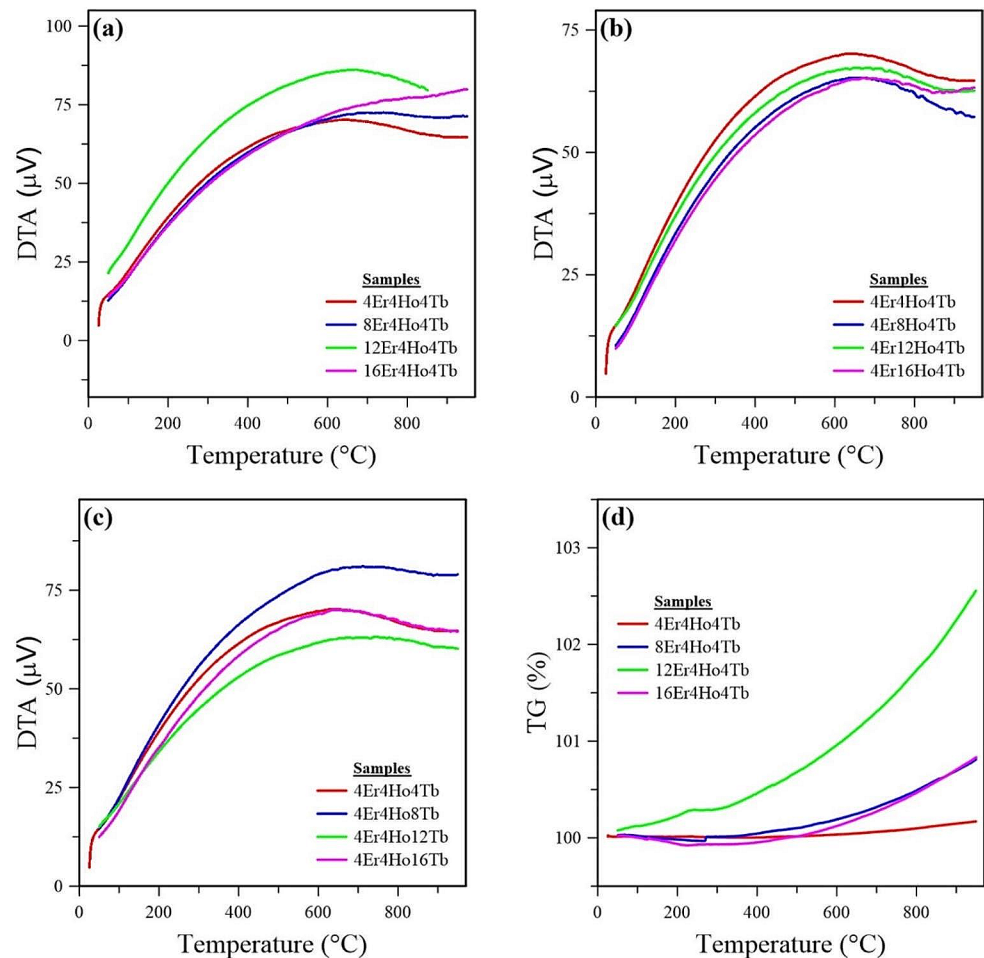
of conductivity with respect to temperature, the following equation arises.

$$\log\left(\frac{\sigma_T}{\sigma_0}\right) / \left(\frac{1000}{T}\right) = -kE_A \tag{5}$$

Starting with Eq. (5), the temperature–dependent conductivity change should be linear, according to the Arrhenius equation. The slope of these Arrhenius plots created between specific temperatures also reveals the electrical activation energy, which gives details on the ion conductivity mechanism of the produced material. The Arrhenius plots of conductivity display a nearly linear change, as seen in Fig. 4a, b, and c. The conductivity curve for some samples, however, bends at about 600 °C. This temperature point is referred to in the literature as an order–disorder transition (ODT), which indicates that mobile oxygen ions in the oxygen sublattice develop a positional arrangement [32–34]. In short, ODT allows some of the O^{2-} ions in the regular 8c areas of the sublattice of the bismuth oxide–based solid crystal lattice to migrate to the 32f regions, which are referred to as intermediate regions. Wachsmann et al.'s

simulation tests on this transition clearly show that above the ODT temperature, the 32 f regions for oxygen mobility require less energy to move to neighboring unoccupied ion centers [35]. Thus, a linear shift is seen before and after the ODT transition, showing two separate ion transport mechanisms in which conductivity is controlled by two separate activation energies, the ones associated with low and high temperature region activation energies.

It is important to note that the high temperature region's (HTR) activation energy is lower than the low temperature region's (LTR) activation energy. This may confirm that oxygen ion mobility is poorer below the ODT temperature and that the fractional distribution of O^{2-} ions to the 32 f region with the transition leads to an increase in mobility [36, 37]. In addition, ODT is not characterized as a phase transition, and therefore it can be said that this transition does not lead to any change in cation positions but only a positional transformation of the ions in the anion sublattice. However, as the doping concentration increases, the gap between HTR and LTR begins to close, and only a single electrical activation energy begins to dominate the lattice. On the other hand, as seen in Fig. 4, conductivity plots move

Fig. 4 Arrhenius plots of conductivity, **a** Er–rich samples, **b** Ho–rich samples, **c** Tb–rich samples **d** Conductivity for Er–rich samples at 700 and 800 °C
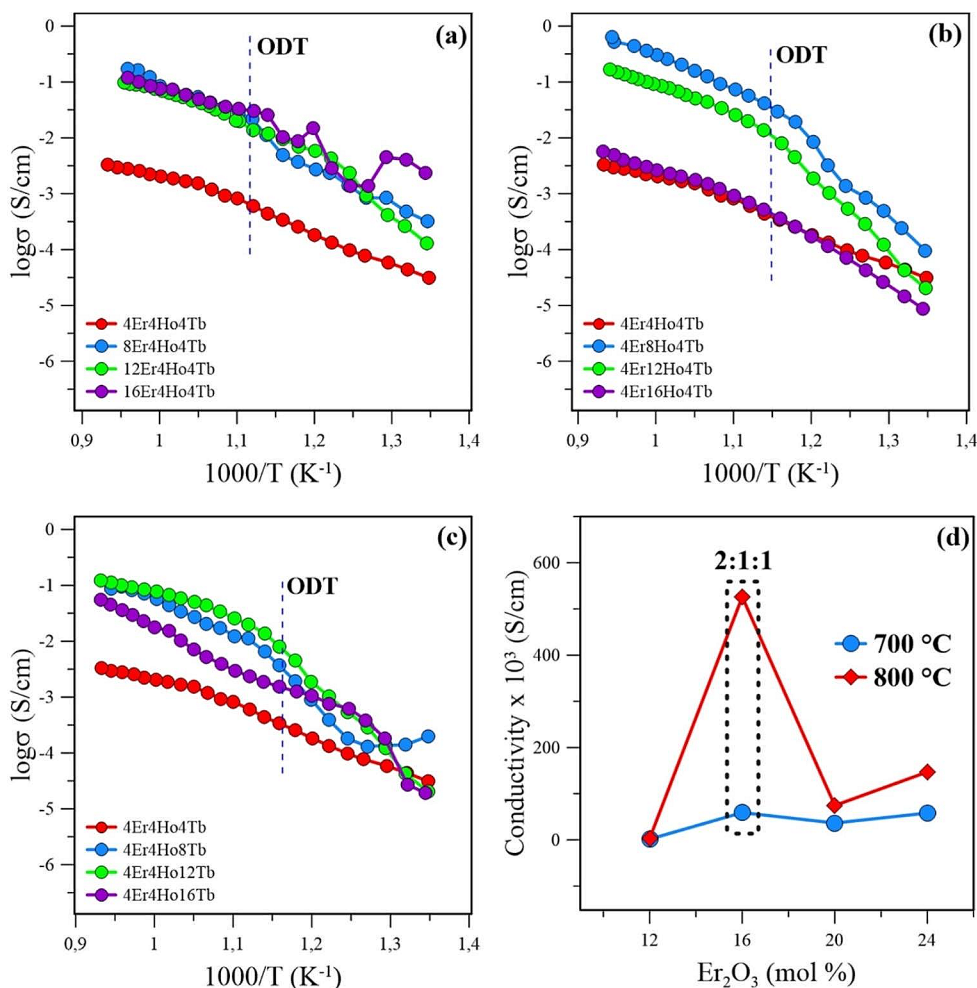
to lower values as the total dopant concentration increases. This is because of the rare earth cations' poor polarizability, which results from a diffusional process in which the host Bi^{3+} cation is partially replaced by the rare earth cations. As a result, it is probable that the quantity of mobile oxygen ions will start to decrease as the number of dopant cations that are occupying the lattice's 4c sites increases and the polarizability continues to decrease. The polarization strength of cations in terms of high conductivity is a crucial feature in this case for the creation of a distorted or deformed oxygen sublattice, which acts as a good environment for oxygen ion mobility [38]. Added to that, doping ions set up in crystal lattice dislocation centers may operate as trapping sites, resulting in a reduction in oxygen ion mobility. It should be noted that these potential cationic trap spots can capture O^{2-} ions, restricting their ion conduction pathways and significantly reducing the quantity of mobile ions that contribute to conduction [39]. Table 3 displays the estimated electrical activation energies as well as the conductivity measurement results. Figure 4d also shows conductivity comparisons for Er–rich samples at 600 and 700 °C.

Table 3 clearly shows that sample 4Er8Ho4Tb has the highest conductivity at 700 °C of all samples, with 0.29 S/cm. It clearly suggests that a 1:2:1 dopant content ratio has an important effect on conductivity [40]. As can be seen in Fig. 4d, the specific ratio results in the best conductivities for Er–rich samples at both 700 and 800 °C. The conductivity of 0.29 S/cm at 700 °C is higher than that of single–doped ESB electrolytes and comparable to the conductivity of 0.56 S/cm reported by Jung et al. The crucial point is that using highly polarizable dopants can aid in obtaining the highest possible conductivity in stabilized Bi_2O_3 materials. It is important to point out that the mentioned ratios (1:2:1, 2:1:1, and 1:1:2) clearly yield successful results for triple–doped Bi_2O_3 systems, as confirmed by this study. As was already mentioned, the data obtained for HTR and LTR show different results with regard to the estimated electrical activation energy. Besides, Table 3 shows that the sample with the highest conductivity, 4Er8Ho4Tb, has the lowest activation energy of 0.44 eV. In oxide–based systems, the activation energy is defined as the lowest amount of energy necessary for an O^{2-} ion in the anion sublattice to hop to nearby unoccupied ion centers [41, 42]. In this way,

Table 3 Conductivity results from measurements and electrical activation energies

Sample abbreviation	Contents ratios	Electrical Conductivity (S/cm)			Activation energy (eV)	
		600 °C	700 °C	800 °C	LTR	HTR
4Er4Ho4Tb	1:1:1	3.40E–04	1.67E–03	3.34E–03	0.50	1.22
8Er4Ho4Tb	2:1:1	4.89E–04	5.91E–02	5.26E–01	0.47	0.71
12Er4Ho4Tb	3:1:1	5.91E–03	3.65E–02	7.45E–02	0.73	0.85
16Er4Ho4Tb	4:1:1	1.03E–02	5.81E–02	14.7E–02	0.84	1.22
4Er8Ho4Tb	1:2:1	2.92E–02	2.92E–01	6.39E–01	0.44	0.69
4Er12Ho4Tb	1:3:1	8.09E–03	8.09E–03	1.94E–02	0.75	0.92
4Er16Ho4Tb	1:4:1	3.60E–04	3.60E–04	1.52E–02	0.50	0.95
4Er4Ho8Tb	1:1:2	3.66E–04	3.66E–04	1.11E–02	0.71	1.14
4Er4Ho12Tb	1:1:3	1.31E–03	2.11E–04	1.06E–02	0.69	1.11
4Er4Ho16Tb	1:1:4	1.60E–04	1.60E–04	6.30E–02	0.61	1.01

disordered anion sublattice at high temperatures can allow for less–demanding ion conduction paths for mobile oxygen ions. On the other hand, sample 4Er4Ho4Tb, which has the lowest conductivity at 700 °C with a conductivity of 0.0016 S/cm, has the greatest activation energy at 1.22 eV. This makes it possible to figure out a close relationship between activation energy and ion conductivity.

Surface analysis

The FE–SEM images of fabricated samples are shown in Fig. 5. The images clearly show that when the dopant concentration increases, the grain boundary and size dramatically change. Besides that, the grain size is not uniform throughout the surface, and as the dopant ratio increases, the grains begin to separate from one another. The observed shrinking in grain size allows the creation of pores on the surface, as seen in the images. It deserves to be noted that the micropores that develop with an increase in doping level can play an essential role in decreasing electrical conductivity. These pores may be actual formations that indicate the impact of doping–induced increased crystal lattice stress on grain dispersion and connectivity to each other [29]. Additionally, lattice strain causes polycrystalline particles to shrink in size, allowing for the emergence of smaller crystal clusters. The creation of the porous structures observed in the images on the grain boundary is inescapable during this crystal aggregation. In terms of the distance of mobile ion conduction pathways, the grain boundary line in a polycrystalline material is crucial due to its effect on the boundary resistance. According to this viewpoint, pores that are generated across the boundary lines may have a blocking impact on the ion conduction paths, resulting in a decrease in conductivity. The images also clearly reveal that the pore density in Tb–rich samples is greater than in Ho–rich and Er–rich samples. This could be why Tb^{4+} cations experience different oxidation levels than Er^{3+} and Ho^{3+} cations.

According to the literature, the Tb^{4+} and Tb^{3+} cations can generate an interstitial defect, which is a kind of point crystallographic defect in which an atom of the same or different type occupies an interstitial position in the crystal structure. The existence of these point imperfections could result in additional stress in the material, which leads to the creation of more pores in the boundary domains [43, 44]. Figure 6 depicts the EDAX pattern of the sample 4Er4Ho4Tb at a distance of 20 μm. This pattern indicates that the combination contains all elements, and there are no peaks indicating impurity atoms. The atom percentage ratio in the mixture approximates the doping stoichiometry.

Conclusions

In conclusion, under air conditions, the Bi_2O_3 compositions co–doped with Er–Ho–Tb were synthesized by means of solid–state reactions and successfully characterized using the XRD, DTA & TG, FPPT, and FE–SEM analytical methods. The XRD patterns indicated that, with the exception of sample 4Er4Ho4Tb, all manufactured samples were cubic δ–phase stabilized at room temperature. The estimated crystal structure variables of the stabilized samples showed that when the dopant concentration increased, the lattice constant decreased, and therefore lattice shrinkage was clearly observed. Additionally, the magnified XRD patterns clearly indicated that as the dopant ratio increased, the (111) plane's primary diffraction peak moved towards higher angles. This angular shift in the diffraction pattern was explained by the decrease in crystal size triggered by doping and partial cation exchanges. The DTA curves exhibited no endothermic or exothermic peaks, indicating a phase transformation, while the TGA curves suggested that weight varied between 1% and 3% depending on temperature. Arrhenius plots of conductivity also confirmed that there is a linear relationship between conductivity and temperature and clearly showed that an increase in the dopant concentration leads to
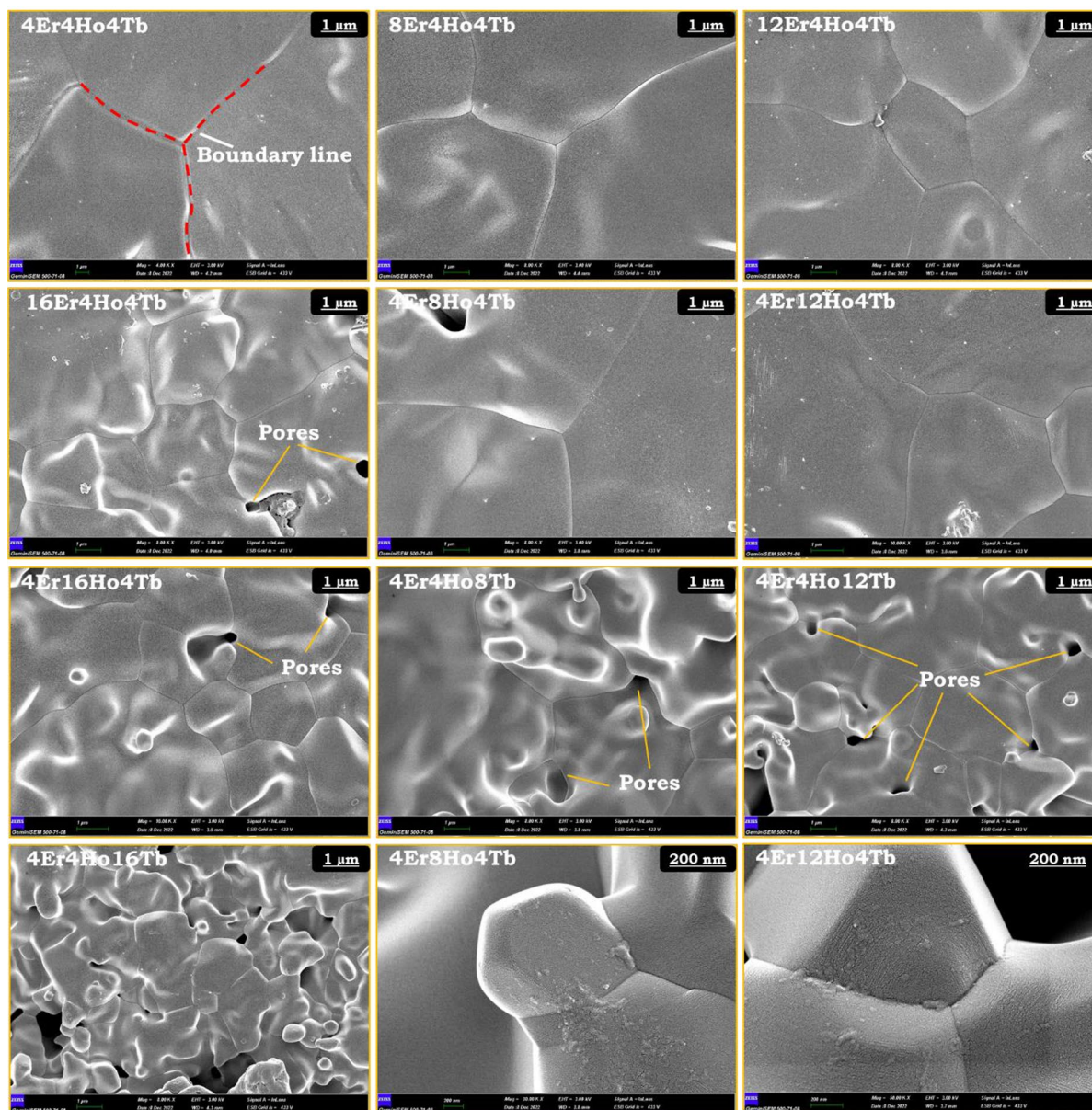
Fig. 5 The FE–SEM images for distance of 1 µm and 200 nm

decay in the conductivity. The highest conductivity, 0.29 S/cm at 700 °C, was achieved in sample 4Er8Ho4Tb, which was fabricated by the 1:2:1 dopant content ratio, which is similar to the ratios suggested by Jung et al. At approximately 600 °C, the ODT effect appeared on the Arrhenius plots, and a division in conductivity graphs was noticed, yielding two different activation energies, LTR and HTR. The activation energies were estimated by computing the slope of the linear fits applied over plots, and they varied from 0.44 eV to 1.22 eV. The FE–SEM images clearly show that the grain size was not uniform and that the grain boundary line turned dramatically with the increasing dopant ratio. Additionally, FE–SEM images of the Tb–rich samples

revealed the development of porous structures at the grain boundaries, which were assumed to play an essential role in the lowering of conductivity. The EDAX pattern of sample 4Er4Ho4Tb, on the other hand, confirmed that all elements utilized as dopants were present in the combination based on the peaks displayed on the pattern.
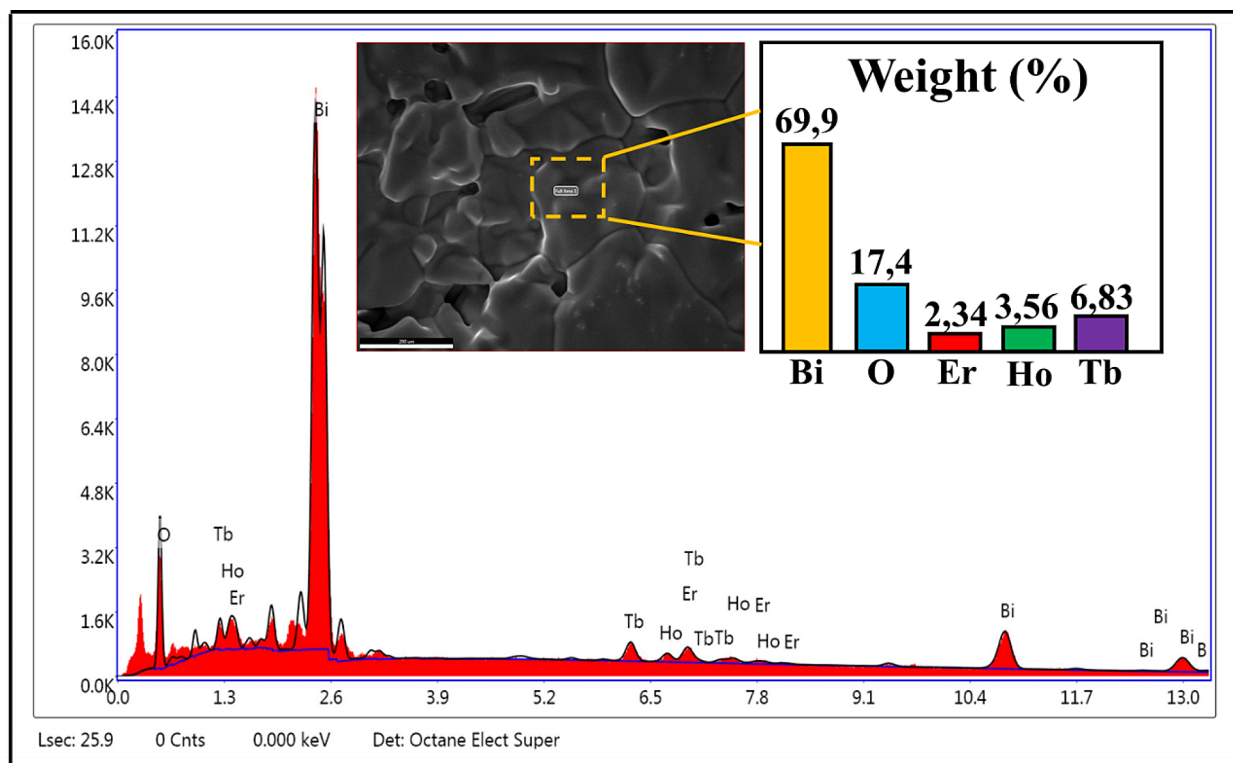
Fig. 6 The EDAX pattern of sample 4Er4Ho4Tb

Declarations

Conflict of interest The authors declare that they have no known competing financial interests or personal relationships that could have appeared to influence the work reported in this paper.

References

1. Singh, M., Zappa, D., Comini, E.: Solid oxide fuel cell: Decade of progress, future perspectives and challenges[J]. Int. J. Hydrog. **46**, 27643–27674 (2021). https://doi.org/10.1016/j.ijhydene.2021.06.020

2. Mahato, N., Banerjee, A., Gupta, A., et al.: Progress in material selection for solid oxide fuel cell technology: A review[J]. Prog Mater. Sci. **72**, 141–337 (2015). https://doi.org/10.1016/j.pmatsci.2015.01.001

3. Zakaria, Z., Hassan, S.H.A., Shaari, N., et al.: A review on recent status and challenges of yttria stabilized zirconia modification to lowering the temperature of solid oxide fuel cells operation[J]. Int. J. Energy Res. **44**, 631–650 (2020). https://doi.org/10.1002/er.4944

4. Wachsman, E.D., Lee, K.T.: Lowering the temperature of solid oxide fuel Cells[J]. Science. **334**, 935–939 (2011). https://doi.org/10.1126/science.1204090

5. Irshad, M., Ain, Q., Siraj, K., et al.: Evaluation of BaZr0.8X0.2 (X = Y, Gd, Sm) proton conducting electrolytes sintered at low temperature for IT–SOFC synthesized by cost effective combustion method[J]. J. Alloys Compd. **815**, 152389 (2020). https://doi.org/10.1016/j.jallcom.2019.152389

6. Hwang, K.J., Shina, M., HyunLee, M., et al.: Investigation on the phase stability of yttria–stabilized zirconia electrolytes for high–temperature electrochemical application[J]. Ceram. Int. **45**, 9462–9467 (2019). https://doi.org/10.1016/j.ceramint.2018.09.026

7. Cardenas, P.S., Ayala, M.T., Muñoz, J., et al.: High ionic conductivity dysprosium and tantalum Co–doped bismuth oxide electrolyte for low–temperature SOFCs[J]. Ionics. **26**, 4579–4586 (2020). https://doi.org/10.1007/s11581-020-03572-y

8. Jolley, A.G., Wachsman, E.D.: A new double Doped Bismuth Oxide with stable ionic conductivity at Intermediate

Temperatures[J]. ECS Trans. **78**, 355 (2017). https://doi.org/10.1149/07801.0355ecst

9. Temluxame, P., Laosiripojana, N., Assabumrungrat, S., et al.: Phase transformation and electrical properties of bismuth oxide doped scandium cerium and gadolinium stabilized zirconia (0.5Gd0.5Ce10ScSZ) for solid oxide electrolysis cell[J]. Int. J. Hydrog. **45**, 29953–29965 (2020). https://doi.org/10.1016/j.ijhydene.2020.08.085

10. Bandyopadhyay, S., Dutta, A.: Thermal, optical and dielectric properties of phase stabilized δ − Dy−Bi2O3 ionic conductors[J]. J. Phys. Chem. Solids. **102**, 12–20 (2015). https://doi.org/10.1016/j.jpcs.2016.11.001

11. Balci, M., Saatci, B., Cerit, S., et al.: The synthesis of Eu–Tb–Ho co–doped Bi2O3–based ceramic powders for use in intermediate temperature–SOFCs[J]. Solid State Ion. **387**, 116060 (2022). https://doi.org/10.1016/j.ssi.2022.116060

12. Ermis, I., Shaikh, S.P.S.: Study of crystallographic, thermal and electrical properties of (Bi2O3)1−x−y(Tb4O7)x(Gd2O3)y electrolyte for SOFC application[J]. Ceram. Int. **44**, 18776–18782 (2018). https://doi.org/10.1016/j.ceramint.2018.07.109

13. Balci, M., Saatci, B., Turk, H., et al.: Effect of ratios of dopant contents on the electrical conductivity of Bi2O3 ceramics co–doped with some rare earth oxides[J]. Mater. Today Commun. **33**, 104542 (2022). https://doi.org/10.1016/j.mtcomm.2022.104542

14. Ayhan, Y.S., Buyukaksoy, A.: Impact of fabrication temperature on the stability of yttria doped bismuth oxide ceramics[J]. Solid State Ion. **338**, 66–73 (2019). https://doi.org/10.1016/j.ssi.2019.05.013

15. Jung, D.W., Lee, K.T., Wachsman, E.D.: Dysprosium and Gadolinium double Doped Bismuth Oxide Electrolytes for low temperature solid oxide fuel Cells[J]. J. Electrochem. Soc. **163**, 411–415 (2016). https://doi.org/10.1149/2.0951605jes

16. Wachsman, E.D., Boyapati, S., Kaufman, M.J., et al.: Modeling of ordered structures of phase–stabilized cubic Bismuth Oxides[J]. J. Am. Chem. Soc. **83**, 1964–1968 (2004). https://doi.org/10.1111/j.1151-2916.2000.tb01498.x

17. Jung, D.W., Juan, C.N., Duncan, K.L., et al.: Enhanced long–term stability of bismuth oxide–based electrolytes for operation at 500°C[J]. Ionics. **16**, 97–103 (2010). https://doi.org/10.1007/s11581-009-0402-9

18. Kanagaraj, T., Sahay, P., Kumar, M., et al.: Novel pure α–, β–, and mixed–phase α/β–Bi2O3 photocatalysts for enhanced organic dye degradation under both visible light and solar irradiation[J]. Environ. Res. **205**, 112439 (2022). https://doi.org/10.1016/j.envres.2021.112439

19. Jung, D.W., Duncan, K.L., Wachsman, E.D.: Effect of total dopant concentration and dopant ratio on conductivity of (DyO1.5)x–(WO3)y–(BiO1.5)1−x−y[J]. Acta Mater. **58**, 355–363 (2010). https://doi.org/10.1016/j.actamat.2009.08.072

20. Wang, X., Zhou, W., De Lisio, J.B., et al.: Doped δ–bismuth oxides to investigate oxygen ion transport as a metric for condensed phase thermite ignition[J]. Phys. Chem. Chem. Phys. **19**, 12749–12758 (2017). https://doi.org/10.1039/C6CP08532F

21. Sundaram, P.S., Sangeetha, T., Rajakarthihan, S., et al.: XRD structural studies on cobalt doped zinc oxide nanoparticles synthesized by coprecipitation method: Williamson–Hall and size–strain plot approaches[J]. Phys. Rev. B Condens. Matter. **595**, 412342 (2020). https://doi.org/10.1016/j.physb.2020.412342

22. Kaschel, F.R., Vijayaraghavan, R.K., Shmeliov, A., et al.: Mechanism of stress relaxation and phase transformation in additively manufactured Ti–6Al–4V via in situ high temperature XRD and TEM analyses[J]. Acta Mater. **188**, 720–732 (2020). https://doi.org/10.1016/j.actamat.2020.02.056

23. Appiah, M., Hao, H., Liu, Z., et al.: The influence of processing methods on the dielectric properties of BaTi1–xGdxO3–x/2

– based materials[J]. Ceram. Int. **47**, 24360–24371 (2021). https://doi.org/10.1016/j.ceramint.2021.05.150

24. Hernández, G.O., Flórez, J.O., Vargas, C.P., et al.: Structural, chemical and electrochemical studies of bismuth oxide thin films growth via Unbalanced Magnetron Sputtering[J]. Surf. Interfaces. **21**, 100627 (2020). https://doi.org/10.1016/j.surfin.2020.100627

25. Fang, W., Yang, T., Huang, K.: In situ synthesis of a high–performance bismuth oxide based composite cathode for low temperature solid oxide fuel cells[J]. Chem. Commun. **55**, 2801–2804 (2019). https://doi.org/10.1039/C9CC00442D

26. Yogamalar, R., Srinivasan, R., Vinu, A., et al.: X–ray peak broadening analysis in ZnO nanoparticles. Solid State Commun[J]. **149**, 1919–1923 (2009). https://doi.org/10.1016/j.ssc.2009.07.043

27. Kuo, Y.L., Liu, L.D., Lin, S.E., et al.: Assessment of structurally stable cubic Bi12TiO20 as intermediate temperature solid oxide fuels electrolyte[J]. J. Eur. Ceram. **31**, 3119–3125 (2011). https://doi.org/10.1016/j.jeurceramsoc.2011.04.039

28. Sadykov, V.A., Koroleva, M.S., Piir, I.V., et al.: Structural and transport properties of doped bismuth titanates and niobates[J]. Solid State Ion. **315**, 33–39 (2018). https://doi.org/10.1016/j.ssi.2017.12.008

29. Boumezoued, A., Guergouri, K., Barille, R., et al.: ZnO nanopowders doped with bismuth oxide, from synthesis to electrical application[J]. J. Alloys Compd. **791**, 550–558 (2019). https://doi.org/10.1016/j.jallcom.2019.03.251

30. Balci, M., Cengel, A., Ari, M.: The microstructure and thermo–electrical characterization of the Tb–Gd–Ho co–doped stabilized Bi2O3 based solid electrolyte systems[J]. Chin. J. Phys. **79**, 89–97 (2022). https://doi.org/10.1016/j.cjph.2022.08.005

31. Elkhoshkhany, N., Mallawany, R.E., Syala, E.: Mechanical and thermal properties of TeO2–Bi2O3–V2O5–Na2O–TiO2 glass system[J]. Ceram. Int. **42**, 19218–19224 (2016). https://doi.org/10.1016/j.ceramint.2016.09.086

32. Chou, T., Liu, L.D., Wei, W.C.J.: Phase stability and electric conductivity of Er2O3–Nb2O5 co–doped Bi2O3 electrolyte[J]. J. Eur. Ceram. **31**, 3087–3094 (2011). https://doi.org/10.1016/j.jeurceramsoc.2011.04.016

33. Bandyopadhyay, S., Dutta, A.A.: Structural insight into the electrical properties of Dy–Ho co–doped phase stabilized Bismuth Oxide based electrolytes[J]. J. Electroanal. Chem. **817**, 55–64 (2018). https://doi.org/10.1016/j.jelechem.2018.03.063

34. Jiang, N., Wachsman, E.D.: Structural Stability and Conductivity of phase–stabilized cubic Bismuth Oxides[J]. J. Am. Ceram. Soc. **82**, 3057–3064 (1999). https://doi.org/10.1111/j.1151-2916.1999.tb02202.x

35. Wachsman, E.D.: Effect of oxygen sublattice order on conductivity in highly defective fluorite oxides[J]. J. Eur. Ceram. Soc. **24**, 1281–1285 (2004). https://doi.org/10.1016/S0955-2219(03)00509-0

36. Rivera, O.D., Martínez, A., Rodil, S.E.: Interpretation of the Raman spectra of bismuth oxide thin films presenting different crystallographic phases[J]. J. Alloys Compd. **853**, 157245 (2021). https://doi.org/10.1016/j.jallcom.2020.157245

37. Emelyanova, Y.V., Krylov, A.A., Kazantseva, A.D., et al.: Bismuth niobates Bi3Nb1 − xErxO7 − δ: Structure and Transport Properties[J]. Russ J. Inorg. Chem. **64**, 151–157 (2019). https://doi.org/10.1134/S0036023619020050

38. Ermis, I., Sertkol, M., Corumlu, V., Inorg, et al.: Nano–Met Chem. **48**, 91–95 (2018). https://doi.org/10.1080/15533174.2016.1157822

39. Balci, M., Ari, M.: A study of the microstructure and thermo–electrical properties of Bi2O3 ceramics co–doped with rare earth oxides[J]. J. Mater. Sci. Mater. Electron. **34**, 534 (2023). https://doi.org/10.1007/s10854-023-09944-0

40. Torun, H.O., Çakar, S.: Thermal characterization of Er–doped and Er–Gd co–doped ceria–based electrolyte materials for SOFC[J].

J. Therm. Anal. Calorim. **133**, 1233–1239 (2018). https://doi.org/10.1007/s10973-018-7189-8

41. Koçyiğit, S.: Boron and praseodymium doped bismuth oxide nanocomposites: Preparation and sintering effects[J]. J. Alloys Compd. **740**, 941–948 (2018). https://doi.org/10.1016/j.jallcom.2018.01.020

42. Wachsman, E.D., Boyapati, S., Jiang, N.: Effect of dopant polarizability on oxygen sublattice order in phase–stabilized cubic bismuth oxides[J]. Ionics. **7**, 1–6 (2001). https://doi.org/10.1007/BF02375460

43. Li, Y., Yang, J., Pan, Z., et al.: Nanoscale pore structure and mechanical property analysis of coal: An insight combining AFM and SEM images[J]. Fuel. **260**, 116352 (2020). https://doi.org/10.1016/j.fuel.2019.116352

44. Aytimur, A., Koçyiğit, S., Uslu, İ., et al.: Fabrication and characterization of bismuth oxide–holmia nanofibers and nanoceramics [J]. Curr. Appl. Phys. **13**, 581–558 (2013). https://doi.org/10.1016/j.cap.2012.10.002